Electronic Supplementary Material (ESI) for Chemical Communications.

Supporting Information for

Mesoporous and carbon hybrid structures from layered molecular precursors for the Li-ion battery application: the case of β-In_2S_3

Ming-Jian Zhang,[‡] Lei-Lei Tian,[‡] Shuankui Li, Ling-Piao Lin and Feng Pan[*]

School of Advanced Materials, Peking University Shenzhen Graduate School, Shenzhen 518055, China

[*]Tel./fax: +86-755-26033200. E-mail: panfeng@pkusz.edu.cn (F. Pan)

I Experimental Section

***Preparation of 2D molecular precursors*:** All chemicals were analytical grade and used as received without further purification. In a typical reaction, 10 mmol Indium powder (1148 mg) and 25 mmol sulfur powder (320 mg) were mixed in 6 ml of 28% ammonia. The mixture was added into a Teflon-lined autoclave with a volume of 25 ml and kept at 180 °C for 5 days. After cooling to room temperature, the obtained product was collected and washed with distilled water. The carbon-coating precursor was obtained by the similar method. Differently, ethylene diamine (En) replaced ammonia as the solvent.

***Preparation of the mesoporous and carbon hybrid samples*:** The mesoporous In_2S_3 sample (denoted as MIS) were obtained by calcinating the carbon-free precursor NH_4InS_2 at 400 °C for 1h in Ar atmosphere. The carbon hybrid In_2S_3 sample (denoted as IS/C) was prepared by calcinating the carbon-containing precursor $EnInS_2$ in the same conditions. Commercial β-In_2S_3 (denoted as IS) was bought as the reference.

***Electrochemical tests*:** The electrochemical performance of the samples was evaluated in Li-ion test cells. The working electrodes were comprised of as-prepared sample, acetylene black and polyvinylidene fluoride (PVDF) with a weight ratio of 3 : 1 : 1. Lithium metal was used as the counter and reference electrodes. The electrolyte was 1 M $LiPF_6$ dissolved in a 1:1:1 mixture of ethylene carbonate (EC), ethylene methyl carbonate (EMC), and dimethyl carbonate (DMC). The cells were assembled in a glove box filled with high-purity argon. Discharge-charge measurements of the cells were performed at different current densities between the potentials of 0.05-3.00 V (*vs* Li^+/Li) on a battery testing system (Neware, Shenzhen). The reported specific capacities are all normalized to the weight of the active materials.

II Measurement and characteristics

X-ray diffraction (XRD) patterns were recorded using a Bruker D8 Advance powder X-ray diffractometer equipped with a rotating anode and using Cu-Kα radiation in the range $10° \leqslant 2\theta \leqslant 80°$. Scanning electron microscopy (SEM) was performed using a Zeiss SUPRA-55 field-emission scanning electron microscope. The crystal structures of these two precursors were determined by a Rigaku Saturn 944+ X-ray single crystal diffractometer. The thermal stability of precursors was characterized by a Mettle Toledo TGA/DSC simultaneous thermal analyzer from room temperature to 900 °C with a heating rate of 10 °C min^{-1}. Transmission electron microscopy (TEM) was performed using a JEOL-2010 instrument at an acceleration voltage of 200 kV. Nitrogen adsorption-desorption measurements were conducted at 77.35 K on an ASAP 2020 analyzer. The Brunauer-Emmett-Teller (BET) surface area was estimated using the adsorption data. The Raman spectrum was measured using a Horiba iHR320 Raman spectrometer with a cooled CCD detector.

III Supplementary tables and figures

Table S1. Crystal data and structure refinement parameters for NH_4InS_2 and $EnInS_2$ ($C_2N_2H_9InS_2$).

chemical formula	NH_4InS_2	$C_2N_2H_9InS_2$
fw	196.98	240.05
cryst size (mm^3)	0.25×0.22×0.05	0.23×0.21×0.06
T (K)	293(2)	293(2)
λ (Mo, Kα, Å)	0.71073	0.71073
cryst syst	Monoclinic	Tetragonal
space group	*C*2/*c* (15)	*I*4(1)/*amd* (141)
a (Å)	11.041(16)	7.764(3)
b (Å)	11.012(15)	
c (Å)	15.50(2)	39.41(2)
β (deg.)	99.99(3)	
V ($Å^3$)	1856(5)	2375.6(19)
Z	24	16
D_{calcd} ($g*cm^{-3}$)	4.229	2.685
μ (mm^{-1})	8.683	4.554
F(000)	2208	1856
θ range (deg.)	2.63–25.30	2.07–25.45
measd. reflns	5932	3730
indep. reflns/ R_{int}	1593/0.2512	606/0.3715
R1[a] ($I > 2\sigma(I)$)	0.2884	0.2593
wR2[b] (all data)	0.6831	0.7481
GOF on F^2	1.012	1.000
$\Delta\rho_{max}/\Delta\rho_{min}$, $e/Å^3$	6.765/-3.987	2.385/-1.607

[a]$R1 = ||F_o| - |F_c||/|F_o|$, [b]$wR2 = [w(F_o^2 - F_c^2)^2]/[w(F_o^2)^2]^{1/2}$.

Notes. There are several alerts of level A in their checkcif files. These alerts could be resulted from two causes below. On one hand, the exact positions of the charge-

balance cations, NH_4^+ and En^+, could not be determined because of their serious disorder distribution between the InS_2^- layers. On the other hand, the diffraction data are not good enough because of the relatively poor crystalline of their single crystals, although multiple single crystals have been tested for them.

Table S2. Bond lengths (Å) and angles (deg.) for NH_4InS_2.

In(1)-S(5)	2.358(17)
In(1)-S(1)	2.372(10)
In(1)-S(4)	2.454(16)
In(1)-S(2)	2.496(12)
In(2)-S(2)#1	2.406(14)
In(2)-S(4)	2.41(2)
In(2)-S(3)	2.474(9)
In(2)-S(5)#2	2.50(2)
In(3)-S(7)	2.13(4)
In(3)-S(2)	2.283(18)
In(3)-S(6)	2.36(4)
In(3)-S(1)#3	2.413(14)
In(4)-S(6)	2.06(3)
In(4)-S(3)	2.295(13)
In(4)-S(7)#2	2.42(4)
In(4)-S(2)#4	2.424(14)
S(1)-In(1)#1	2.372(10)
S(1)-In(3)#5	2.413(14)
S(1)-In(3)#6	2.413(14)
S(2)-In(2)#1	2.406(14)
S(2)-In(4)#6	2.424(14)
S(3)-In(4)#1	2.295(13)
S(3)-In(2)#1	2.474(9)

S(5)-In(2)#7	2.50(2)
S(7)-In(4)#7	2.42(4)
S(5)-In(1)-S(1)	109.8(6)
S(5)-In(1)-S(4)	105.4(7)
S(1)-In(1)-S(4)	110.2(6)
S(5)-In(1)-S(2)	110.9(7)
S(1)-In(1)-S(2)	110.0(3)
S(4)-In(1)-S(2)	110.4(5)
S(2)#1-In(2)-S(4)	112.0(5)
S(2)#1-In(2)-S(3)	109.2(3)
S(4)-In(2)-S(3)	111.8(6)
S(2)#1-In(2)-S(5)#2	106.4(6)
S(4)-In(2)-S(5)#2	107.7(6)
S(3)-In(2)-S(5)#2	109.6(5)
S(7)-In(3)-S(2)	104.3(10)
S(7)-In(3)-S(6)	120(2)
S(2)-In(3)-S(6)	104.5(10)
S(7)-In(3)-S(1)#3	111.2(15)
S(2)-In(3)-S(1)#3	108.4(5)
S(6)-In(3)-S(1)#3	107.5(10)
S(6)-In(4)-S(3)	107.0(9)
S(6)-In(4)-S(7)#2	121(2)
S(3)-In(4)-S(7)#2	102.7(10)
S(6)-In(4)-S(2)#4	110.1(13)
S(3)-In(4)-S(2)#4	108.0(5)
S(7)#2-In(4)-S(2)#4	107.3(12)
In(1)#1-S(1)-In(1)	110.2(6)
In(1)#1-S(1)-In(3)#5	109.1(3)

In(1)-S(1)-In(3)#5	109.1(3)
In(1)#1-S(1)-In(3)#6	109.1(3)
In(1)-S(1)-In(3)#6	109.1(3)
In(3)#5-S(1)-In(3)#6	110.3(7)
In(3)-S(2)-In(2)#1	111.5(5)
In(3)-S(2)-In(4)#6	112.4(7)
In(2)#1-S(2)-In(4)#6	108.9(5)
In(3)-S(2)-In(1)	109.3(5)
In(2)#1-S(2)-In(1)	106.8(6)
In(4)#6-S(2)-In(1)	107.7(4)
In(4)-S(3)-In(4)#1	113.2(7)
In(4)-S(3)-In(2)	108.3(2)
In(4)#1-S(3)-In(2)	110.1(3)
In(4)-S(3)-In(2)#1	110.1(3)
In(4)#1-S(3)-In(2)#1	108.3(2)
In(2)-S(3)-In(2)#1	106.6(5)
In(2)-S(4)-In(1)	106.3(7)
In(1)-S(5)-In(2)#7	106.8(7)
In(4)-S(6)-In(3)	123(2)
In(3)-S(7)-In(4)#7	118(3)

Symmetry codes: (#1) -x+2, y, -z+1/2; (#2) x-1/2, y+1/2, z; (#3) x+1/2, y+1/2, z; (#4) -x+5/2, y+1/2, -z+1/2; (#5) x-1/2, y-1/2, z; (#6) -x+5/2, y-1/2, -z+1/2; (#7) x+1/2, y-1/2, z.

Table S3. Bond lengths (Å) and angles (deg) for $EnInS_2$.

In(1)-S(1)	2.431(6)
In(1)-S(3)	2.468(6)
In(1)-S(2)	2.544(5)
In(1)-S(2)#1	2.544(5)

S(1)-In(1)#2	2.431(6)
S(2)-In(1)#3	2.544(5)
S(3)-In(1)#4	2.468(6)
S(1)-In(1)-S(3)	104.9(3)
S(1)-In(1)-S(2)	106.48(16)
S(3)-In(1)-S(2)	113.42(12)
S(1)-In(1)-S(2)#1	106.48(16)
S(3)-In(1)-S(2)#1	113.42(12)
S(2)-In(1)-S(2)#1	111.45(17)
In(1)-S(1)-In(1)#2	106.3(4)
In(1)-S(2)-In(1)#3	101.9(3)
In(1)-S(3)-In(1)#4	103.5(3)

Symmetry codes: (#1) -y+3/4, x-1/4, -z+1/4; (#2) -x+0, -y+1/2, z+0; (#3) y+1/4, -x+3/4, -z+1/4; (#4) -x+1, -y+1/2, z+0.

Table S4. The EDX results for NH_4InS_2 and $EnInS_2$.

Elements	atom% in NH_4InS_2	atom% in $EnInS_2$
N	24.3	38.7
In	25.6	21.5
S	50.1	39.8

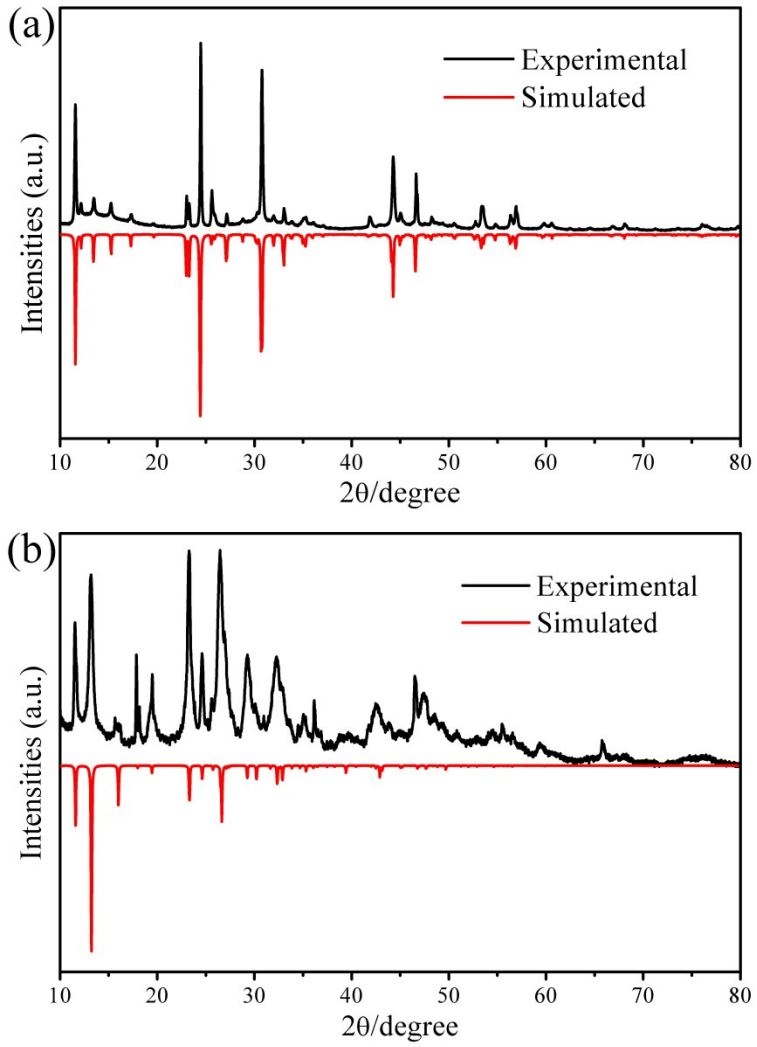

Fig. S1 The experimental and simulated powder XRD patterns of NH_4InS_2 (a) and $EnInS_2$ (b).

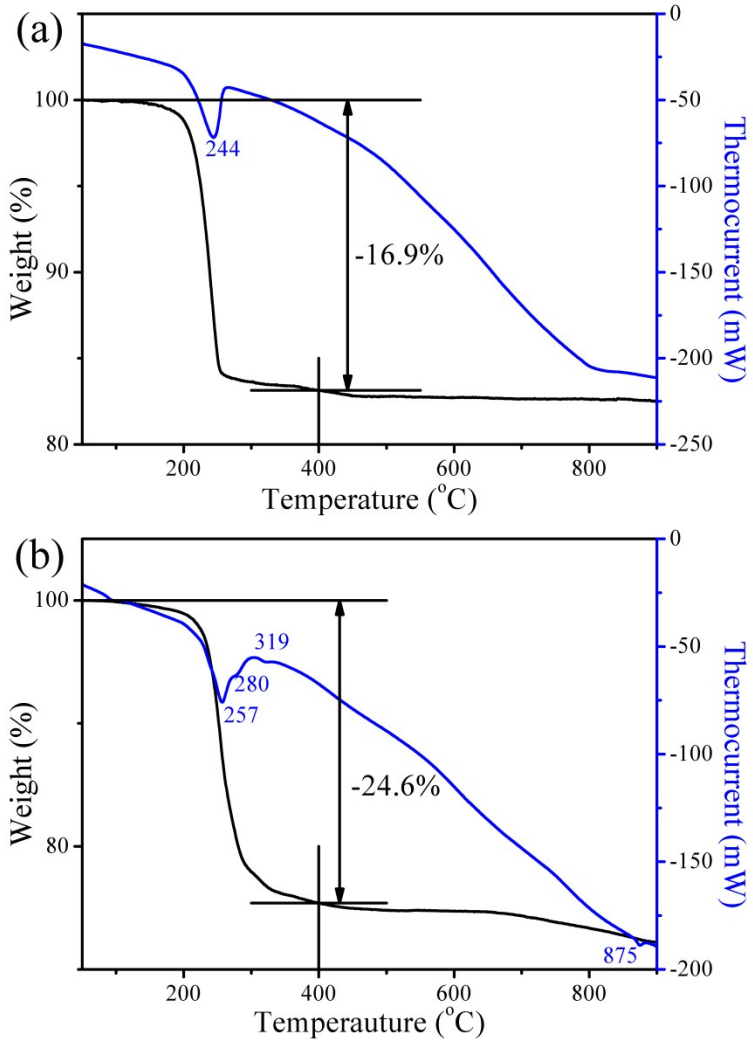

Fig. S2 The TG curves of NH_4InS_2 (a) and $EnInS_2$ (b).

In order to evaluate the thermal stability of these two precursors, the thermogravimetric (TG) analysis was performed (Fig. S2). As shown in Fig. S2a, the weight loss is 16.9% when the temperature rises up to 400 °C, which is basically consistent with the theoretical weight loss (17.3%) from NH_4InS_2 to In_2S_3. There is just one exothermic peak at 244°C, which could be ascribe to a quick weight loss process due to the release of NH_3 and H_2S. As shown in Fig. S2b. the weight loss is 24.6% at 400 °C, which is lower about 8% than the theoretical weight loss (32.7%) in the decomposition from $EnInS_2$ to In_2S_3. Accordingly, the pyrolysis carbon content in the IS/C sample could be estimated as about 12%. There are three exothermic peaks before 400 °C in the thermocurrent curve, indicating the presence of the multiple

decomposition steps.

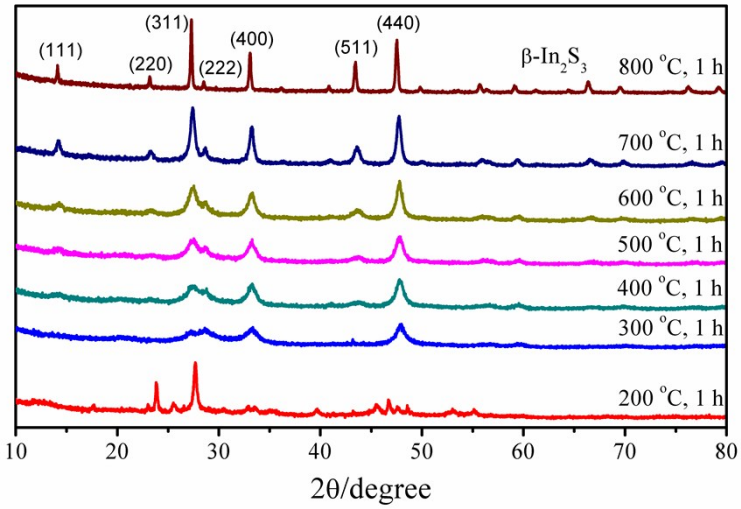

Fig. S3 The varied temperature powder XRD patterns of NH_4InS_2.

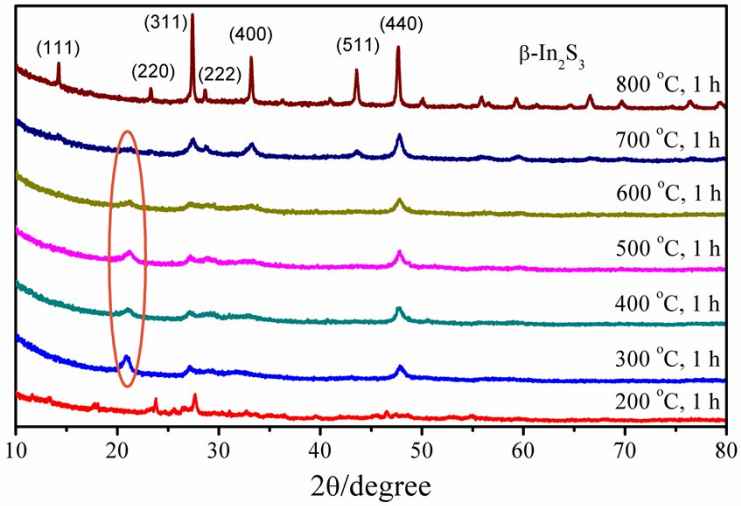

Fig. S4 The varied temperature powder XRD patterns of $EnInS_2$.

The varied-temperature powder XRD was carried out to illuminate the phase conversion of NH_4InS_2 and $EnInS_2$ in the thermal decomposition process (Fig. S3 and S4). As shown in Fig. S3, when the temperature rises up to 200 °C, the intensities of many peaks significantly decrease, and two new peaks at about 24 and 28 degree show up compared with the origin pattern, indicating that the decomposition has occurred. This is consistent with the TG analysis above. When the temperature goes up to 300 °C, the original framework has been destroyed completely and converted

into the framework of β-In_2S_3 because of the appearance of (311), (400) and (440) peaks. The intensities of these three peaks gradually increase with the rising temperature, hinting a better crystallinity. Differently with NH_4InS_2, there was a new peak at about 21 degree at 300 °C (Fig. S4) for $EnInS_2$. It could be assigned to the pyrolysis carbon from the interlayer En. It gradually decreases with the rising temperature, and disappears at 800 °C. This is consistent with the color change of the sample from gray to red. Owing to the multiple sintering at the increasing temperature, the pyrolysis carbon is gradually oxided into CO_2. Notably, there is another totally different phenomenon between the patterns of NH_4InS_2 and $EnInS_2$. The intensities of three main peaks, for (311), (400) and (440) lattice planes of β-In_2S_3, were basically unchanged before 700 °C for $EnInS_2$. They significantly increase until 700 °C and 800 °C, accompanied with the disappearance of the pyrolysis carbon. This phenomenon demonstrates that the pyrolysis carbon could greatly hinder the growth of β-In_2S_3 from the small crystalline grain into the large crystalline grain.

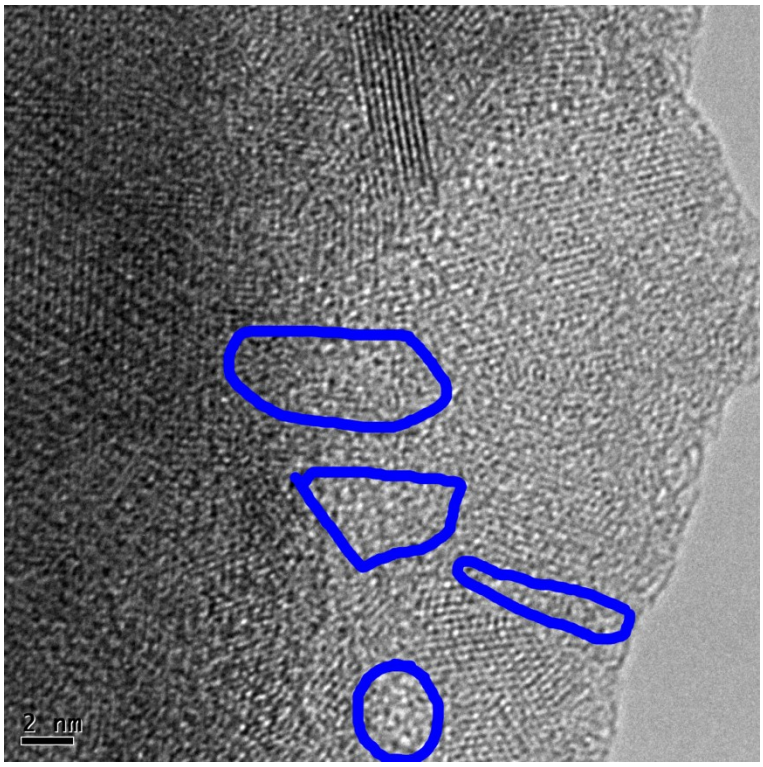

Fig. S5 HRTEM image of the IS/C sample.

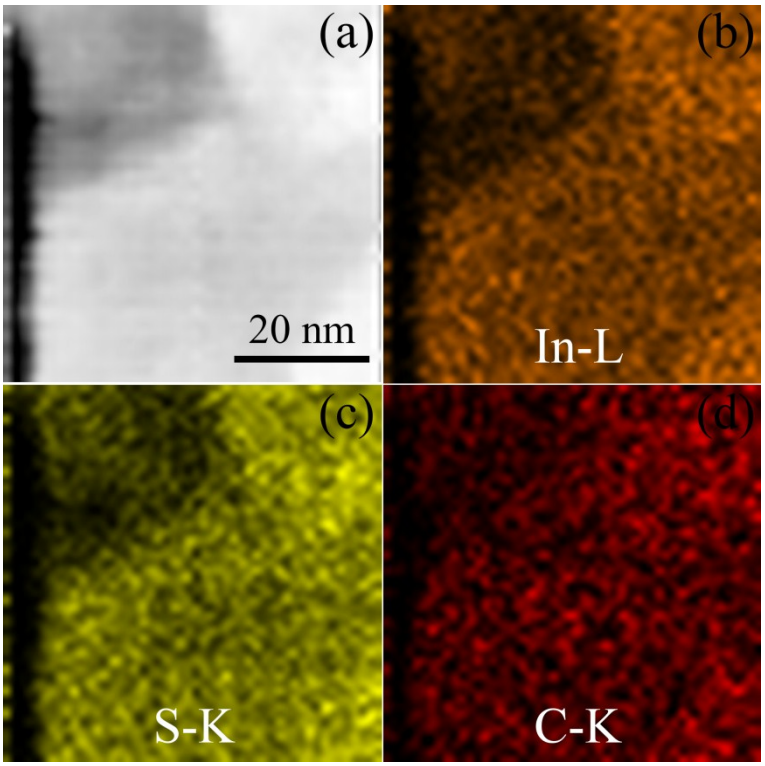

Fig. S6 HAADF-STEM image (a), In-L EDX map (b), S-K EDX map (c) and C-K EDX map (d) of the IS/C sample.

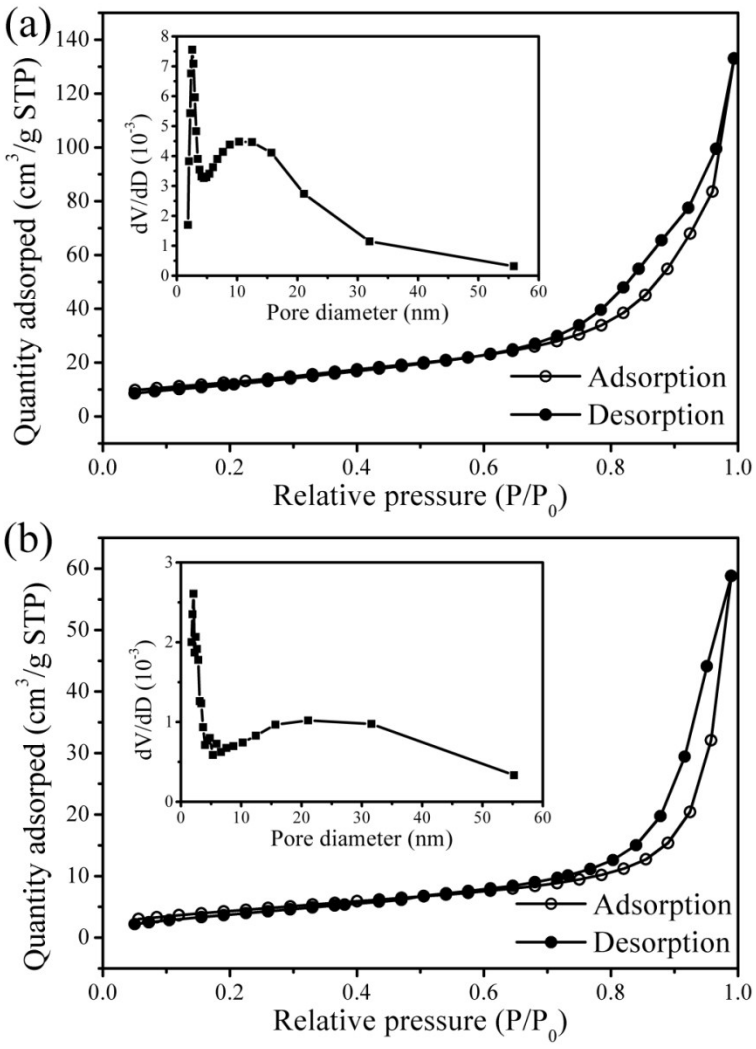

Fig. S7 The N_2 adsorption-desorption isotherm of the MIS (a) and IS/C (b) samples. The insets show the corresponding pore size distribution curves calculated by BJH equation in the adsorption branch.

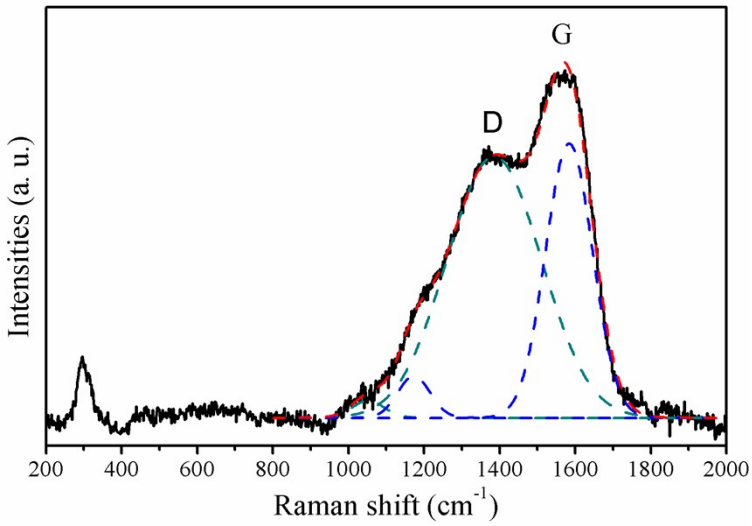

Fig. S8 Raman spectrum of the IS/C sample.

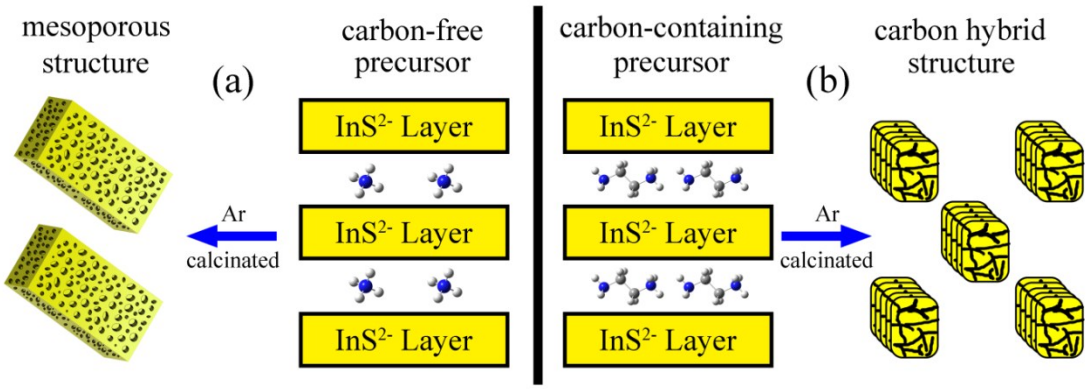

Fig. S9 Schematic diagrams for the preparation process from the carbon-free layered precursor to the mesoporous structure (a), and from the carbon-containing layered precursor to the carbon hybrid structure (b).

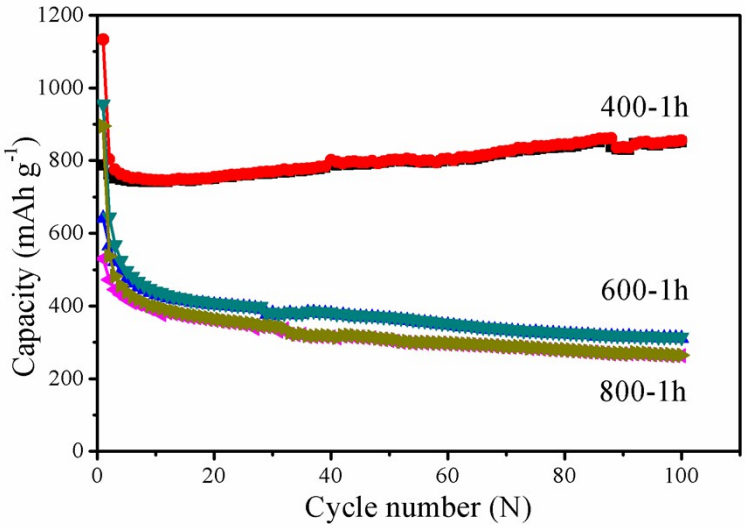

Fig. S10 Cycling performance at current density of 0.1 A g^{-1} for three IS/C samples sintered at 400, 600 and 800 °C for 1 hour, respectively.

As shown in Fig. S10, the calcination temperature was found to be an important factor to obtain high-performance anode materials. It is obvious that the cycling performance of IS/C sample greatly decreased with the increasing temperature from 400 to 600 and 800 °C. This phenomenon might be partly ascribed to the decrease of the carbon content (Fig. S2a). More importantly, the improved bulk crystallinity of In_2S_3 from 400 to 800 °C shown in Fig. S4 and the distribution of pyrolysis carbon could also bring into the great decrease of cycling performance.